Allosteric action of nucleotides on Hsp90 across several time- and length scales

Steffen Wolf*†,[1] Benedikt Sohmen†,[2] Björn Hellenkamp*,[2,3] Johann Thurn,[2] Gerhard Stock,[1] and Thorsten Hugel*[2,4]

[1)] *Biomolecular Dynamics, Institute of Physics, University of Freiburg, Freiburg, Germany*

[2)] *Institute of Physical Chemistry, University of Freiburg, Freiburg, Germany*

[3)] *Engineering and Applied Sciences, Columbia University, New York, USA*

[4)] *Signalling research centers BIOSS and CIBSS, University of Freiburg, Freiburg, Germany*

(Dated: 12 March 2020)

In allosteric communication, signals are mediated by an effector and propagate from its binding site to distant functional sites of the protein. Several indicators for such allostery caused by hydrolysis of bound ATP have been found in the Hsp90 dimer. Joining single molecule fluorescence-based methods with extensive atomistic molecular dynamics simulations, this work aims to establish a simple model of allosteric information transfer from the nucleotide binding site to the overall dimer. Hydrolysis of one ATP effects a structural asymmetry in the full dimer that leads to the collapse of a central folding substrate binding site. Arg380 is the major mediator in transferring structural information from the nucleotide to the substrate binding site. The allosteric process occurs via hierarchical dynamics that involve timescales from pico- to milliseconds and length scales from Ångstroms to several nanometers. We presume that similar hierarchical mechanisms are fundamental for information transfer through proteins.

I. INTRODUCTION

Allosteric communication is a general mechanism for the regulation of protein function and signalling, as it enables alteration of protein structures at active sites by small changes in a binding pocket several nanometers away.[1–3] In spite of its importance as elementary process of cell signalling, there is surprisingly little known about the underlying dynamical process and the timescales of allosteric communication.[4–8] Understanding of the molecular mechanisms of allostery is crucial to, e.g., elucidate the effects of point mutations in cancer development[9] and exploit it for the design of small molecule drugs.[10]

In this work, we investigate allostery within the structure of the yeast molecular chaperone heat shock protein 90 (Hsp90). Hsp90 is highly conserved in eucariotic cells, being involved in many intracellular signalling pathways,[11,12] serving for example as a cyclin-dependent kinase regulator, and is therefore a target protein for cancer treatment.[13,14] Hsp90 is a homodimer consisting of two copies from a 670 amino acid protein, with each of the chains containing three domains named N, M and C (see Fig. 1). The two monomers undergo large conformational changes, which are usually classified into N-terminal open and closed states.[15] A nucleotide binding site is found within the N-domain (see Fig. 1a). Structural changes on the Ångstrom scale such as the hydrolysis of ATP into ADP are believed to cause significant conformational changes of the full dimer.[11,12] Several models with atomistic resolution are available for the closed state: X-ray crystallography structures of yeast Hsp90 bound to the co-chaperone Sba-1 and the non-hydrolysable nucleotide AMPPNP (PDB ID 2CG9),[15] the endoplasmatic reticulum Hsp90 analogue Grp94 with a folding substrate-mimicking polypeptide and AMPPNP (5ULS),[16] the mitochondrial Hsp90 TRAP1 with AMPPNP (4IPE, 4IYN, 4J0B and 4IVG)[17] and a cryo-EM structure of the human Hsp90 dimer bound to ATP with the co-chaperone Cdc37 and the kinase Cdk4 as folding substrate (5FWK and 5FWL).[18] Further representative conformations of the functional cycle are found in form of the partially closed Grp94 (2O1U, 2O1V, 2O1W, and 2O1T).[19] Structures of the open state have been proposed based on molecular dynamics (MD) simulations[20–22] and by a combination of single molecule Förster resonance energy transfer (smFRET) and MD simulations.[23] Despite this wealth of structural information, the molecular details on how nucleotides affect the dimer and how the nucleotide hydrolysis cycle is coupled to folding client binding and processing have remained elusive.[24]

Here, we report on a joint experimental and theoretical study combining smFRET, fluorescence correlation spectroscopy (FCS) and fluorescence lifetime measurements with fully atomistic MD simulations to investigate allosteric communication in Hsp90 across several time- and length scales. Intensity-based smFRET has been used to determine conformational dynamics and distances in (bio)polymers for more than 20 years.[25–31] More recently, single molecule lifetime and anisotropy measurements have been added to increase the range of accessible timescales and characterise physicochemical properties of fluorophores.[31,32] We use both methods to determine distances between selected amino acid side chains in the M-domain of Hsp90 and investigate distance changes upon addition of different nucleotides. Complementary, we perform unbiased and biased all-atom MD simulations of the full dimer in a physiological NaCl solution and

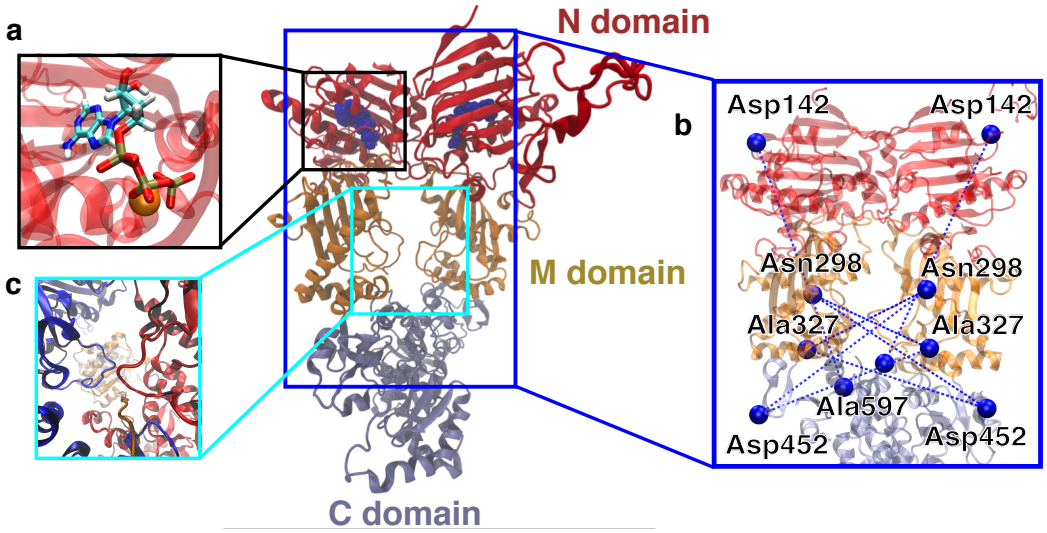

Fig. 1. Overview of the Hsp90 dimer. The displayed structure is the initial protein model based on the X-ray crystal structure 2CG9.[15] N-domain is shown in red, M-domain in orange, C-domain in light blue. **a** Nucleotide (in sticks) binding site in the N-domain. Magnesium ion as orange sphere. **b** FRET distance pairs. **c** Overview of the central folding substrate binding site. Protein dimer (blue and red) and Cdk4 (orange) in the active folding complex in the cryo-EM structure 5FWK.[18]

loadings of different nucleotides (total simulation length of 25 μs) to obtain insights into molecular mechanisms which are not directly accessible with smFRET.[33–35] We find that Arg380, which has been assumed to be involved in the functional cycle before,[36–38] is a prominent residue for the transfer of allosteric information. Experimentally and computationally observed time- and length scales of allosteric communication agree well with each other, which allows us to propose a detailed molecular pathway from hydrolysis to a large conformational change of the M-domains.

II. RESULTS AND DISCUSSION

Intermolecular distance measurements. To describe the effect of nucleotides on the closed conformation of the Hsp90 dimer, we performed smFRET experiments. We attached pairs of Atto550 and Atto647N fluorophores to all combinations of the amino acid positions 298, 327 and 452 as well as the amino acids 142 and 597 (see the blue network in Fig. 1b). Three out of four of the labels are located in the middle domain of the protein dimer, i.e., between M-M and M-C domains at a distance of 3.0-5.0 nm from the nucleotide binding site. 142-597 is a complementary N-C distance pair. Each FRET label pair was measured in the apo form and additionally in the presence of 2 mM ATP, ADP, AMPPNP or ATPγS (see Methods). In a previous study[23] we focussed on the open ADP bound state and the closed AMPPNP state, and determined the dynamics of the Hsp90 domains on the millisecond timescale. Here we focus on the N-terminal closed states of Hsp90 under various nucleotide conditions. Choosing suitable FRET pairs, we can now distinguish two closed states of Hsp90. Using information from fluorescence lifetime and fluorescence correlation experiments we also found position-specific dynamics on the low-µs timescale, which can be connected to timescales observed in MD simulations.

Several of the investigated protein/nucleotide complexes clearly show three populations of preferred distances. These populations can be attributed to the existence of two closed protein structures (termed closed states A and B) in addition to the open protein conformation (see Fig. 2a,b). Even for the nucleotide conditions with a low populated closed state B, fits with three populations represent the data well (Fig. 2c). The two closed populations are consistent with several previous studies on yeast Hsp90,[41–43] HtpG[44] and Grp94.[45] The closed states can be best distinguished in the presence of AMPPNP where they are most populated. Therefore we used the mean FRET efficiencies of the three states from the AMPPNP data to constrain fits of other nucleotides. The width of the fits was not constrained as these three global states are dynamic and might show nucleotide dependent fine structure due to small structural differences (see below). The averaged apparent distances between the dyes $R_{\langle E \rangle}$[31] and their distributions are extracted by Photon Distribution Analysis (PDA)[39,40] for separation of distance distributions from shot-noise (see Methods for details and Supplementary Table 1 for all measured distances).

To access molecular details of the population shifts observed in smFRET, we performed MD simulations of the Hsp90 dimer with different nucleotides bound (Supplementary Tab. 2). We checked if simulations reached

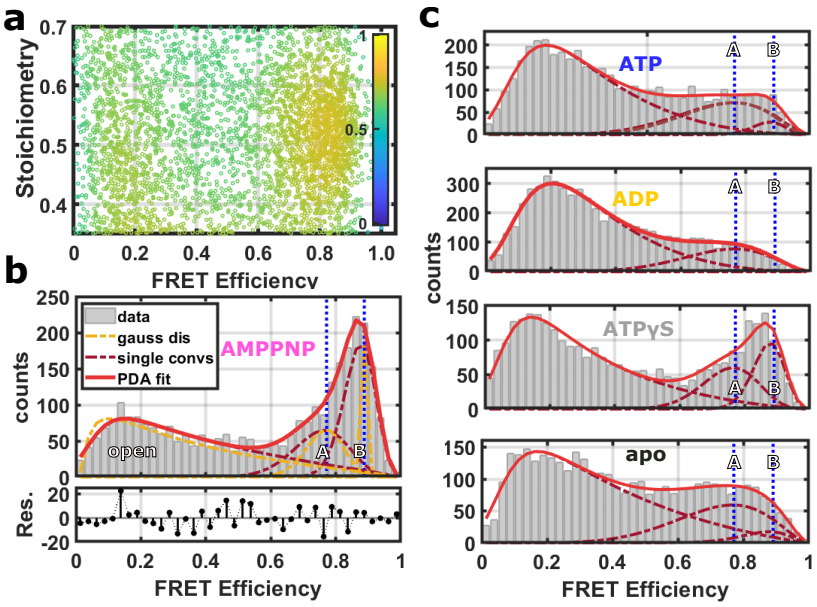

Fig. 2. Single-molecule FRET data analysis exemplarily shown for the distance 298-327 (see Supplementary Fig. 1 for distances 298-452, 327-452 and 142-597). **a** Corrected 2D FRET efficiency vs. stoichiometry histogram in the Hsp90 dimer with AMPPNP. A kernel density estimator was used to visualise the burst density by colour. **b** FRET efficiencies between the dyes and their distributions are extracted by Photon Distribution Analysis (PDA),[39,40] which includes a separation from shot-noise. For the 298-327 distance the PDA fit (red line) results in three states (dark red dashed lines): an open state, a closed state, termed closed state A and a more contracted closed state termed closed state B. For each population the mean distance μ was obtained from the shot-noise filtered distributions (orange lines) as expectation values (indicated by vertical blue dashed lines). **c** Each FRET efficiency was measured under five different nucleotide conditions. Here, PDA fits with three fixed mean distances between the dyes are shown.

an equilibrated state after initial relaxation by assessing the time traces of the C_α root mean square displacement (RMSD) of the initial secondary structure elements within the full dimer (excluding the charged loop at sequence positions 208 to 280) and the radius of gyration of the full protein. As an example, Supplementary Fig. 2 displays the structural development of the global protein in a representative ATP-bound simulation. For all simulations, the first structural development away from the initial state appears to be completed after 0.5 µs.

Nucleotide binding. As a first step towards an understanding of the structural differences imposed by the nucleotides onto the protein, we focused on structural changes found directly at the nucleotide binding sites in simulations. Figure 3a shows a representative structure of ATP bound after 1 µs simulation time. ATP is stably connected to the protein at Asp79 via the adenine moiety. The magnesium ion is α, β, γ-coordinated via the triphosphate, and bound to the protein via Asn37, which in turn forms a hydrogen bond with P_α. The P_γ phosphate forms a stable salt bridge with Arg380. In our simulations, Arg380 is positioned directly at the tetrahedron surface of P_γ that needs to be accessed by an attacking water molecule, and thus Arg380 in this position effectively shields the triphosphate from hydrolysis. This shielding could explain earlier experimental findings that ATP bound to Hsp90 in either the open or closed protein conformation exhibits a life time in the range of several seconds.[46]

In comparison to this arrangement, we observe significant deviations in the simulations with ADP + P_i (see Fig. 3b). In the case of the doubly hydrolysed state with two ADP + P_i (in the following abbreviated as ADP), the binding mode of the adenine moiety and the magnesium ion is unaffected. $P_{\alpha,\beta}$ still coordinates the magnesium ion, but P_i serves as additional bidentate coordination partner. Its position interferes with the positioning of the Arg380 side chain, pushing it away from $P_{\alpha,\beta}$. Furthermore, the free phosphate disrupts a salt bridge of Arg380 and Glu33. This particular glutamate has been shown to be involved in the ATPase activity of Hsp90, as well.[47,48] Arg380 in turn is highly conserved within the family of Hsp90 and its homologues[24,49] and has been reported as a major player in ATP hydrolysis.[21,50] Previously, Arg380 has indeed been considered as a potential residue to mediate the stabilisation of a specific N/M arrangement.[36] Furthermore, it was shown that a R380A mutant completely suppresses the formation of the closed state.[37,38] Finally, in the apo form, the binding site exhibits (at least transiently) a collapsed state, moving all mentioned protein residues closer together. Glu33 and Arg380 again are found in a salt bridge, but the position

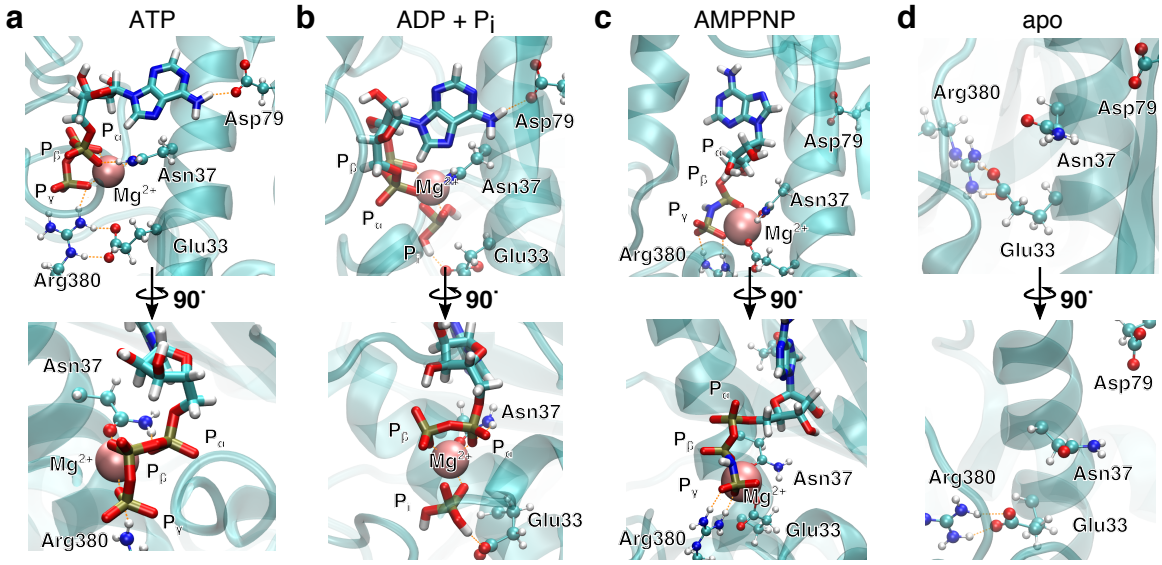

Fig. 3. Nucleotide binding site in **a** ATP-bound, **b** ADP + P_i-bound, **c** AMPPNP-bound and **d** apo-Hsp90 simulations after 1 µs. Nucleotides displayed as sticks, amino acid side chains as balls and sticks, protein backbone as cartoon, hydrogen bonds as orange dashes. In the case of ADP + P_i, Arg380 has left the nucleotide binding site.

of Arg380 is significantly different from the one in the nucleotide-bound state.

Interestingly, the binding mode of AMPPNP (Fig. 3c) is significantly different from the one of ATP. The ribose moiety in one of the two monomers is flipped completely by about 180°. The binding mode of the adenine moiety of AMPPNP becomes instable in three out of five simulations (see Supplementary Tab. 2), and the P_γ-Arg380 salt bridge ruptures in one simulation. Furthermore, only P_β and P_γ coordinate the magnesium ion. This effect appears to be caused by the presence of a new hydrogen bond donor in form of the NH group between P_β and P_γ that forms contacts with surrounding polar residues, as well as due to changes in charge distribution within the triphosphate resulting from the heteroatom substitution. Instead, Glu33 becomes part of the coordination sphere of the magnesium ion, disrupting the Glu33-Arg380 salt bridge.

To investigate the effect of the hydrolysis of only a single ATP molecule, we performed simulations with one ATP and one ADP + P_i bound, respectively (in the following abbreviated as ATP/ADP). In this case the binding mode of the adenine "anchor" residue of ADP is stable in three out of the five simulations (see Supplementary Tab. 2), while in the remaining simulations one or both anchors lose their contact with Asp79, respectively.

Structural changes of the Hsp90 dimer. To connect smFRET measurements and MD simulations, we calculated the expected distance distributions $P\left(R_{\langle E\rangle}\right)$ for fluorophore pairs directly from intraprotein dye-accessible volumes of the simulated structures (see Methods). In this way, we can directly compare simulations with the measured mean distances and uncertainties.

Figure 4a shows the means and uncertainties extracted from the experimental FRET efficiency histograms (see Fig. 2, Supplementary Fig. 1 and Methods for details). State A occurs at distances comparable to the ones found within the crystal structure 2CG9, state B represents a structure in which the protein has significantly contracted, and does not correspond to any previously structurally described state. At the start of the simulation we observe a qualitative agreement with experiment for distances attributed to the closed states A under all nucleotide conditions. In the case of ATP and AMPPNP, the simulation mainly stay in state A. However, in the presence of ATP/ADP and even more clearly in the presence of ADP, the distributions show some tendency towards closed state B. Missing convergence of MD simulations to state B indicates structural relaxation timescales longer than the maximal single trajectory length of 1 µs.

To accelerate structural changes leading to closed state B and to overcome the timescale limitations of unbiased simulations, we employed nonequilibrium targeted MD simulations[51,52] with implicit solvent for one of the ADP simulations and pulled the C_β distances of amino acid pairs 298-327, 298-452 and 327-452 towards each other (see Methods for details). The targeted MD distance distributions indeed evolve towards the experimentally measured distances (see Fig. 4a, bottom). The $R_{\langle E\rangle}$ of these three pairs agree well with their experimental counterparts. The 142-497 distance pair, which we did not manipulate, also tends towards its closed state B.

We observe that ATP generally tends to narrow distance distributions and larger overall distances, indicating that closed state A is most stable with ATP (before hydrolysis) and opens a central hole between the monomers (see below). All other states (even including AMPPNP) tend to wider distributions and/or cover

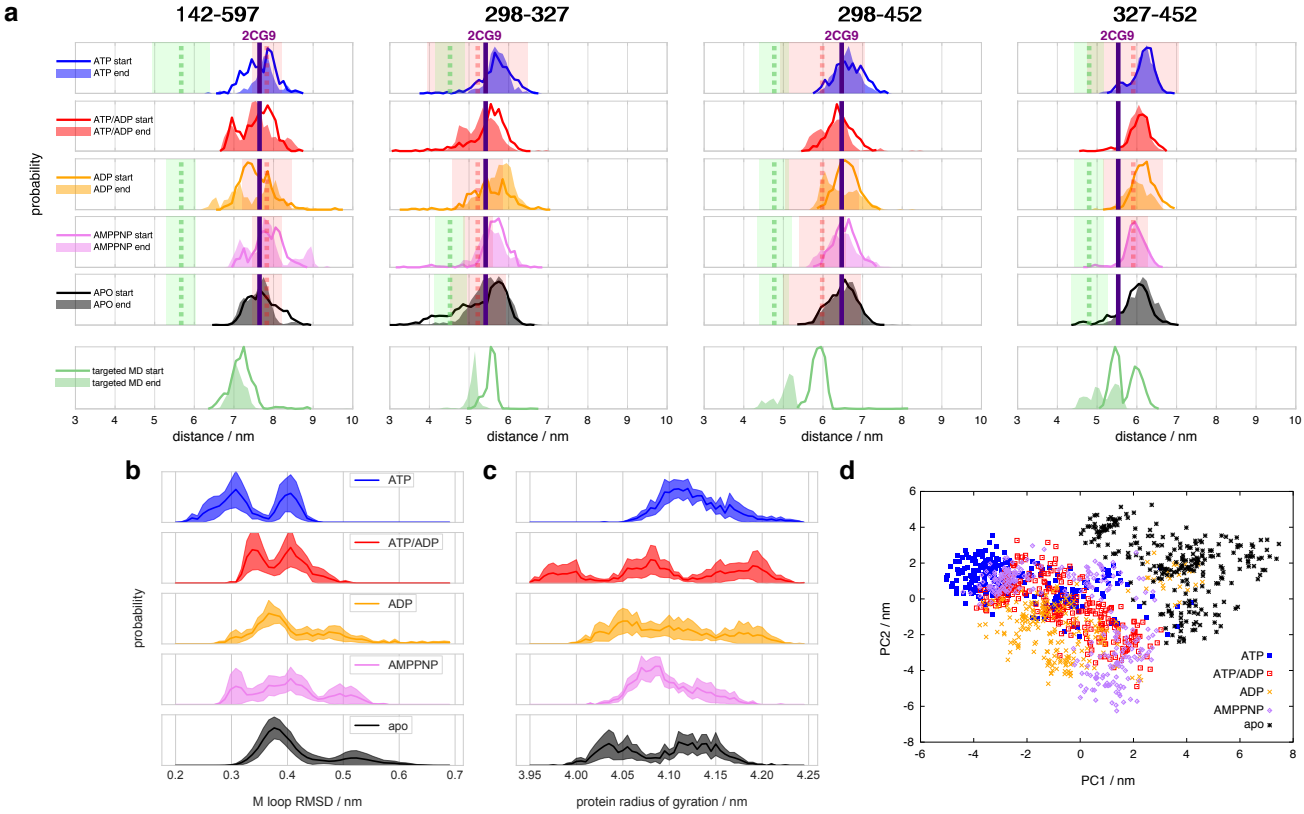

Fig. 4. Histograms of selected Hsp90 distances. **a** Experimental and simulated apparent distances $R_{\langle E \rangle}$ of the FRET label pairs 298-327, 298-452, 327-452 and 142-597 (see Methods for details). Line histograms display the first 0.25 µs of simulation (termed "start"), filled histograms the last 0.25 µs (termed "end"). Vertical dashed red and green lines indicate the measured mean distances ($R_{\langle E \rangle}$) of closed states A and B, respectively, and coloured transparent areas the respective uncertainties from experiment (see Supplementary Tab. 1). The vertical purple line indicate the 2CG9 structure state distance.[15] Targeted MD represent the first and last 0.25 ns of calculations, respectively, starting from an ADP state after 1µs of unbiased MD. **b** RMSD of internal M-domain loop (sequence positions 323 to 340) during the last 0.25 µs with reference to positions in the active folding complex determined via cryo-EM (5FWK).[18] **c** Radius of gyration of the full protein during the last 0.25 µs of simulation. **d** Principal component (PC) analysis of the last 0.5 µs of simulations of intraprotein contact distances within nucleotide binding sites and M-loops.

shorter distances that develop towards closed state B, i.e., towards closing the hole.

Does this change in M-M distances have a functional consequence at other sites of the protein? To address this question, we compared our MD results to the Hsp90-Cdk4 cryoEM-structure (PDB ID 5FWK).[18] Fig. 1c shows that the peptide chain of the partially unfolded client Cdk4 passes right through the core of the dimer between the two M-domains. The chain is held in place by two loops coming out of the M-domains (sequence positions 323-340).[18] To compare the M-loop structures appearing during simulation to the corresponding cryo-EM structure, Fig. 4b displays the respective C_α-RMSDs. The ATP-bound structure appears to switch between two conformations, one of which (RMSD $\approx$ 0.3 nm) is closest to the cryo-EM structure loop arrangement. Interestingly, AMPPNP resembles more the hydrolysed states than ATP. We further note that these M-loops are found at a distance of ca. 4.0 nm, i.e., quite far away, from the nucleotide binding site.

To assess structural differences of the full protein effected by different nucleotides, we also analyse the differences in the radius of gyration of the full dimer in Fig. 4c. The ATP-bound protein tends to a clearly defined large radius of gyration, while all other investigated states display a broader distribution and trend to smaller radii. Again, AMPPNP states resemble more the hydrolysed states. ATP binding apparently causes Hsp90 to adopt an extended closed conformation when the M-domains are considered. Such an extension in combination with a restriction of the accessed conformation space would lead to both a decreased solvent and conformational entropy. The resulting entropic penalty could be compensated by the enthalpic contributions of bound ATP, with hydrolysis leading to a return into a wider range of closed conformations with a decreased radius of gyration.

Allosteric communication between nucleotide binding site and the protein dimer. To identify the

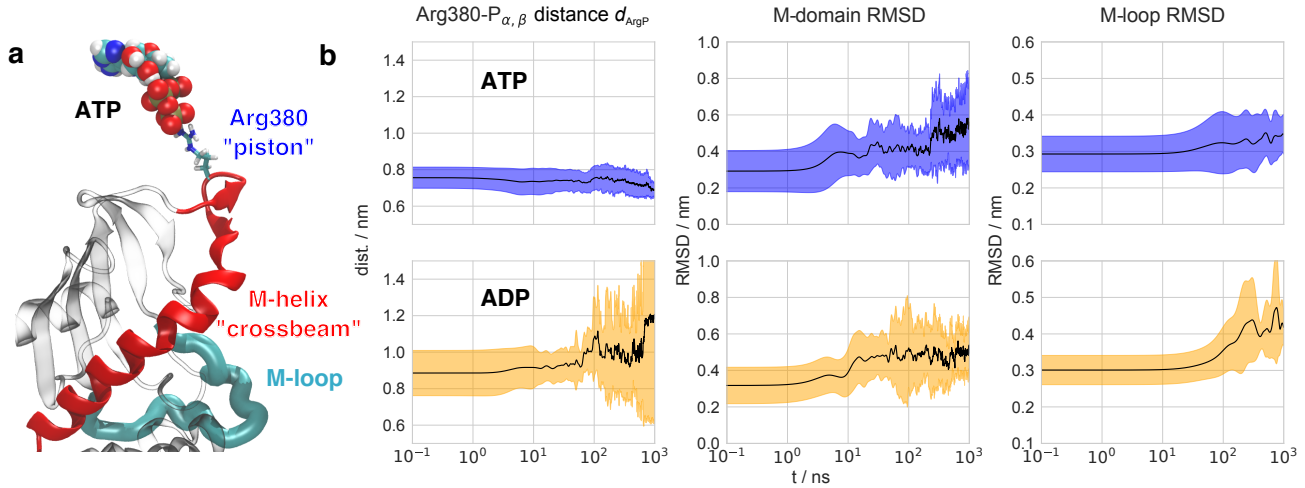

Fig. 5. Transfer of structural changes from the nucleotide binding site to the full protein dimer. **a** Essential mechanistic coupling of nucleotide binding site and the M-domain. ATP as van der Waals spheres, Arg380 "piston" as sticks, M-domain helix "crossbeam" (residues Leu374 to Glu408) in red, M-loop in cyan, remaining M-domain in grey (other monomer not shown). **b** Time evolution of average structural changes observed in ATP and ADP state simulations, respectively. Mean values displayed in black lines, standard deviations as coloured traces. Displayed observables are: distance between the Arg380 CZ atom (center atom of guanidinium group) and the respective nucleotide P_α/P_β mass center; RMSD of the Cα atoms from secondary structure elements (helices, sheets) in the M-domain after fit of the respective N-domain Cα atoms from secondary structure elements (helices, sheets); RMSD of the two internal M loops in respect to the conformation of the substrate bound cryo-electron microscopy structure (PDB ID 5FWK).[18]

key amino acids responsible for the structural information transfer, we performed a correlation-based principal component analysis (PCA) on the contacts[53,54] made by amino acids forming the nucleotide binding site and the M-loop (see Methods for details). The principal components display linearly independent combinations of inter-residue distances weighed according to their individual contribution to explain the correlation of distance changes in the analysed set of contacts. Hence, they can serve as "reaction coordinates" to elucidate the mechanism of structural information transfer. Figure 4d displays trajectories of the various systems projected onto the resulting first two principal components. The principal components clearly separate apo- and ATP-states. AMPPNP, ATP/ADP and ADP partially cover the ATP- and apo-states, but also areas that neither correspond to the latter two states, which is in qualitative agreement with our results given above.

Investigating the importance of individual contacts on the first two principal components (Supplementary Fig. 3), we find that besides changes within the binding pocket and the M-loop, Arg380 is highlighted to exhibit pronounced changes as found above. Arg380 is indeed prominent with respect to allosteric communication, as it is the only residue which reaches into the nucleotide binding site, but is also part of the M-domain.

On the basis of this insight, Fig. 5a shows the key structural elements of a mechanistic model of allostery. Arg380 forms a salt bridge with the P_γ of ATP, and is positioned in a loop at the N-terminal end of a helix (sequence positions 376-408, in the following called M-helix), which is part of the M-domain. The helix runs across the face of the central β-sheet of the M-domain, and thus can apply tension and affect the position of the whole domain. The location of the M-domain position in turn affects the orientation of the M-loop and thus regulates the formation of the folding client binding site. In other words, Arg380 serves as a "piston" to connect ATP and the N-terminal end of the M-helix via electrostatic interactions. The M-helix in turn represents a "crossbeam" that exerts force on the M-domain and effects the formation of the folding client binding site.

It is instructive to consider the effect of this mechanistic coupling on the different nucleotide states (Supplementary Fig. 4a-c). In the ATP-bound state, we observe that the Arg380–P_γ salt bridge is present in both monomers. Arg380 pulls on the M-helices in both monomers, resulting in a very symmetric dimer structure. In the case of ATP/ADP, on the other hand, the free phosphate stays within the binding site and disturbs the position of one of the two Arg380 side chains. In this case, Arg380 moves away from the nucleotide, relieving the tension applied to the M-helix in the respective monomer. The Arg380 side chain in the other monomer with ATP still pulls in its M-helix. The resulting imbalance in connectivity between both monomers introduces a structural asymmetry, which has been observed to exist in other experiments.[17,55,56] In the case of full hydrolysis (ADP), the retraction of Arg380 from the nucleotide binding site is present for both monomers, likely recovering structural symmetry. We emphasise that the structural symmetry of the protein seen here is not effecting

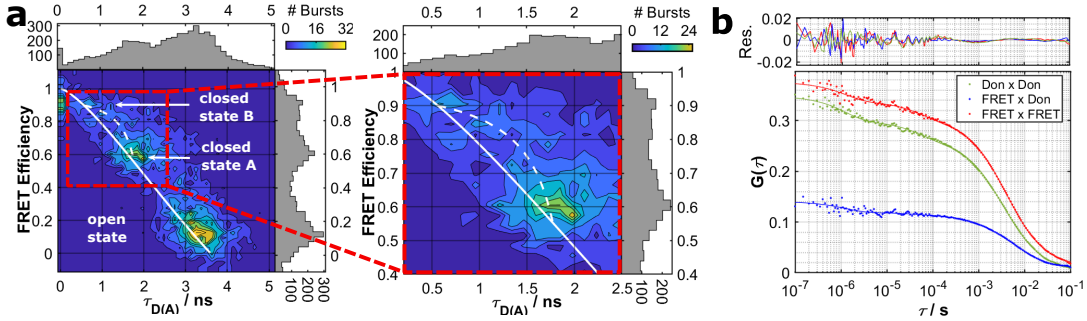

Fig. 6. Microsecond to millisecond kinetics revealed by fluorescence-based techniques. **a** Donor lifetime in the presence of the acceptor $\tau_{D(A)}$ vs. FRET efficiency E analysis from single-molecule-experiments. Shown are E vs. $\tau_{D(A)}$ for the FRET pair 298-452 in presence of AMPPNP. Three FRET populations can be identified. The largest $\tau_{D(A)}$ can be associated to the open state and the shorter $\tau_{D(A)}$'s to the two closed states, respectively. The static FRET line is depicted as white solid line, the dynamic FRET line between the two closed states as white dashed curve. FRET bursts on the dynamic line indicates fast kinetics between the two closed states. **b** FRET-FCS analysis for the FRET pair 298-452 in the presence of AMPPNP. Correlations of the parallel and perpendicular donor signal (green), FRET signal (red) and the cross-correlation of the parallel FRET signal with the perpendicular donor signal (blue) are shown. A global fit with two kinetic terms revealed dynamics on the timescale of about $1\mu s$ and $60\mu s$, respectively (see Supplement Figs. 5-8 for details and additional data).

a symmetry in ATP hydrolysis. ATP hydrolysis appears to be a stochastic event, leading to the ATP/ADP state as the most probable post-hydrolysis structural intermediate.

It is interesting to note that in the proposed mechanism, the major role of ATP is the addition of electrostatic interactions to the chaperone, stabilising a client-binding competent conformation via induced structural stress. This hypothesis is in line with the observation that ATP exhibits a comparatively long life time in the binding pocket.[46] Hydrolysis then returns the chaperone into an inactive state with a wide range of accessible conformations and, from a thermodynamic perspective, completes the overall energetic balance for the folding process. We therefore hypothesise that ATP acts as a regulatory element activating Hsp90 similar to GTP in GTPases,[57] instead of directly performing work on the folding client.

The allosteric communication suggested here differs from the one proposed for the bacterial homolog of Hsp90, HtpG,[20] as the involved structural elements (in particular the N-domain) differ significantly between HtpG and yeast Hsp90. Our observation that ATP hydrolysis shifts the equilibrium between the two closed states towards the more contracted state agrees well with a recent EPR study on yeast Hsp90[43]. In addition, recent simulations on human Hsp90 have implicated the loop region around Arg380 to take part in allosteric communication as well, but were too short to observe the structural changes discussed here.[58]

Time evolution of structural changes in MD simulations. The model of allosteric communication in Hsp90 developed above suggests a sequence of information flow from the nucleotide binding site to the folding client binding site. To test this idea, we perform a time series analysis of our trajectories. Based on our findings above, the simulation starting structure is a mixture between an ATP-like and a partially hydrolysed state. We therefore consider the ADP trajectories as equilibration simulations from a non-equilibrium starting structure after hydrolysis. To monitor intra-protein changes associated with this allosteric communication, we focus on (i) the distance d_{ArgP} between the Arg380 side chain guanidinium carbon atom and the $\mathrm{P}_{\alpha,\beta}$ mass center, (ii) the C_α-RMSD of M-domain position (using C_α-atoms of the N-domain as fit reference) and (iii) the C_α-RMSD of the M-loop arrangement (residues 323-340) in reference to the cryo-EM structure 5FWK. Observable d_{ArgP} highlights changes within the binding pocket directly after hydrolysis at a distance of $\sim$ 0.4 nm from the triphosphate, the M-domain RMSD protein report on conformational changes at intermediate ($\sim$ 2.0 nm) distance, and the M-loop RMSD reflects conformational changes at the folding client binding site ($\sim$ 4.0 nm distance).

Figure 5b displays the time evolution of means and standard deviations of these observables for ATP and ADP, averaging over 5 trajectories in each case. In the following, we discuss the apparent changes according to their timescales. A complementary visualisation of changes in ADP simulations is given in Supplementary Movie 1. The first differences appear directly at the start of simulations at $t \lesssim 1$ ns: in ATP simulations, d_{ArgP} is constant and exhibits only small fluctuations at all times. The simulations with ADP start with an increased d_{ArgP} ($\sim$ 0.15 nm longer) and exhibit larger fluctuations, reflecting a motion of Arg380 away from the nucleotide caused by the mobile free phosphate. These differences are a result of the different nucleotide structures in the simulations, and appear directly in the initial structure minimisation. In experiment, this conformational change is expected to occur following hydrolysis on a sub-ns timescale.

The detachment of Arg380 from the nucleotide is a prerequisite for the subsequent rearrangements of the M-domain, which occur on a 10 ns timescale. In fact, at $t \gtrsim 10$ ns, the M-domain RMSD in the ADP system abruptly rises to ca. 0.5 nm. This change corresponds to an increased flexibility of the M-helix, followed by a rotation of the M-domains (see Supplementary Movie 1). For ATP/ADP (see Supplementary Fig. 4d), we find a similar increase in M-domain RMSD, which appears to be slowed down and completes after 100 ns, pointing to a residual stabilisation of the active folding conformation from the single bound ATP. Indeed, mutants of Hsp90 have been reported that only allow the delayed hydrolysis of a single ATP molecule, but still retain the capability to fold substrates.[59] We mention that also in the ATP simulations an initial increase in M-domain RMSD to ~ 0.4 nm takes place at similar times, followed by a delayed jump to a value similar to the one in the ADP simulations at ca. 300 ns. We interpret this change to come from the ATP simulations undergoing structural changes towards the folding-competent state. This involves conformational changes that are different from the one in the ADP simulations, but apparently follow a similar sequence of events.

The rotation of the M-domains is a prerequisite for the collapse of the folding client binding site, which is indicated by the M-loop RMSD and appears for $t \gtrsim 100$ ns. While the mean RMSD increases to ca. 0.35 nm in ATP, it reaches ca. 0.45 nm in ADP, which is in agreement with the distance-resolved RMSD profile in Fig. 4b. Lastly, d_{ArgP} strongly increases after $t = 0.8$ µs in ADP and exhibits large fluctuations. On longer timescales ($t > 1$ µs), these overall fluctuations may coincide with a destabilisation of the N-N interface and thus the opening of the dimer.[23]

The observed process timescales apparently follow a logarithmic scale, which is a hallmark of hierarchical dynamics, where fast processes associated with small free energy barriers regulate slow transitions:[60,61] changes of the Arg380 position within $\lesssim 1$ ns cause M-domain rearrangements on a 10 ns scale, which in turn are followed by sub-µs conformational changes of the M-loops forming the folding client binding site. The missing convergence to state B-associated distances implies that the full transfer from state A to the proposed state B takes even longer. Indeed, already the relaxation of small proteins from nonequilibrium states involves timescales of tens of microseconds and beyond,[8] and thus is outside of the scope of current unbiased MD simulation techniques.

Timescales observed from lifetime and FRET-FCS data. Motivated by this *in silico* timescale analysis, we investigated on which timescales dynamics can be observed in our experimental data. First we tested for sub-ms dynamics by FRET efficiency vs. fluorescence lifetime plots.[62,63] Fig. 6 reveals signatures of dynamics on fast timescale between the closed states A and B (here depicted for the 298-452 FRET pair with AMPPNP). The open protein conformation can be identified as population with the largest donor lifetime and lowest FRET transfer rate, and the closed conformational states A and B as the two populations with low donor lifetimes and high FRET efficiencies. The solid white diagonal in Fig. 6 represents the theoretically calculated static FRET line (see Methods). That is, if the states do not exchange on fast timescales, all populations should be found on this line. Focusing on the two closed populations, we can also calculate the dynamic line (dotted curve), which represents dynamic exchange between the two closed states on a sub-ms timescale. We emphasise that the dynamic line is not the result of a fit, but an analytic solution, with only the two end points required to be fixed to the FRET efficiencies of the two closed states.[62–64] Comparing the measured data to these limiting cases, the zoom in Fig. 6a shows that the data clearly fits better to the dynamic line.

To further investigate the fast fluctuations, we performed FRET-FCS measurements.[65,66] We calculate the autocorrelation and cross-correlation functions of the donor fluorescence and the FRET-induced acceptor signal (see Fig. 6b). A thorough analysis (see Methods) suggests correlation times on three timescales. The first correlation time on the order of a few milliseconds corresponds to the diffusion time of Hsp90. The two other correlation times most likely correspond to structural dynamics within the Hsp90 dimer. The estimated timescales of the found dynamics are in the range of $\tau_L \approx 50 - 200$ µs and $\tau_K \approx 1 - 4$ µsand are shown for two FRET pairs and all nucleotide conditions in Supplementary Fig. 5-8. The fast timescale τ_K agrees well with the slowest timescale seen in our MD simulations for closure of the folding substrate binding site, while τ_L fit well with our proposed slow conversion from closed state A into closed state B and with the interconversion of closed states A and B seen in FRET-lifetime data.

While the presented channel of allosteric communication transfers structural information from the nucleotide to the M-domains, it only forms a small part of possible allosteric interactions within the dimer. For example, it is known that Trp300 appears to transfer structural information on folding client binding to the M-domains.[67] Intriguingly, Trp300 is found on a loop domain that lies exactly on the opposite face of the central β-sheet of the M-domain to the one facing the M-helix. We speculate that client contacts with Trp300 thus may assist the M-helix in pulling the M-domains into the folding-capable conformation, and antagonize the structural compaction upon ATP hydrolysis presented here. Another recently reported allosteric switch for the regulation of Hsp90 function is found in Lys594 at the C-C domain interface.[68]

Structural model of state B from targeted MD simulations. To obtain a model for the structural changes underlying τ_L and τ_K, we evaluate the data from our biased MD simulations (see Methods for details). The structural consequences are displayed in Supplementary Fig. 9 and in the Supplementary Structure set: one of the monomers gains a kink at its M-C in-

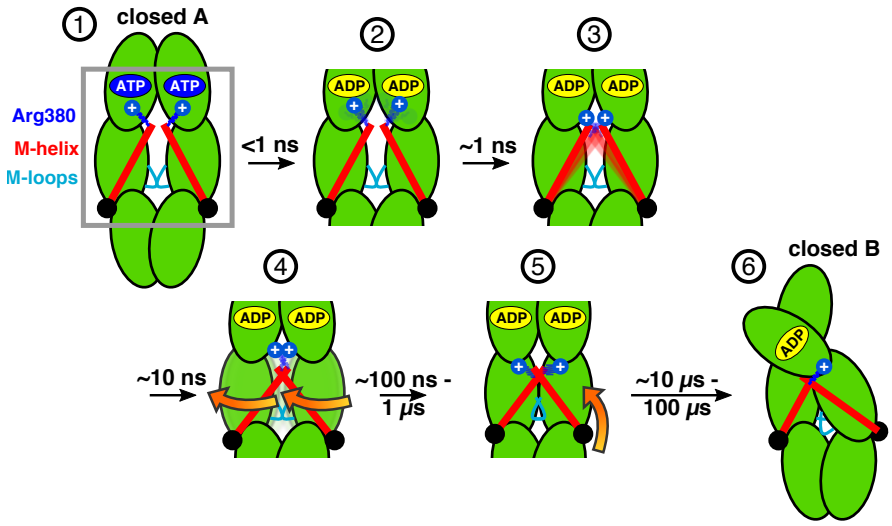

Fig. 7. Scheme of allosteric communication including timescales. Steps 1–5 can be observed in unbiased MD simulations, steps 5 and 6 are in agreement with smFRET and FRET-FCS data and targeted MD simulations. Note that our data indicate that the hydrolysis of one ATP is already sufficient to induce the structural changes towards closed state B (see Supplementary Fig. 4). See Supplementary Figure 9 for a structural model of the closed state B.

terfaces and bends over towards its partner monomer, resulting in an asymmetric contracted state, which we tentatively attribute to represent a structural model of closed state B. This asymmetric state, in which one of the two monomers significantly differs in its form from its neighbor, has so far not been described.

III. CONCLUSIONS

We are now in a position to formulate a model of allosteric communication involving Arg380 and the M-helix depicted as steps (1)-(6) in Fig. 7: starting with ATP (1), Arg380 forms a salt bridge with P_γ, and the resulting electrostatic interaction is transmitted via the M-domain to the M-loops, keeping the folding substrate binding site open. In the following steps, sub-ns hydrolysis cleaves the connection between nucleotide and piston (2), the strain exerted by the M helix on the M-domains is lost within a nanosecond (3), and within about 10 ns the protein relaxes into an entropically favorable distribution of conformations (4) that form contracted states on a timescale of several hundred nanoseconds, where the M-domains are closer to each other and have rotated (5). Finally, on the timescale of several hundreds of µs the dimer contracts into the asymmetric state B (6). Such hierarchical timescales for the individual steps in this allosteric communication hint towards a rugged free energy landscape involving several tiers underlying this transition.[8,61] Comparing this structural evolution with the crystal structure 2CG9, we note that 2CG9 appears as a hybrid between the ATP state (judged by the FRET distances) and the ADP state (judged by the position of the M-domains and the M-loop). This mixture of states might originate from AMPPNP and an allosteric effect of the co-chaperones bound to the N-domains in 2CG9.

For the design of chemotherapeutics, novel inhibitors of Hsp90 could thus be based on creating small organic molecules that occupy the Arg380 position in the N-domain or interfere with the Glu33-Arg380 salt bridge or that pull on Arg380, similar as to the action of ATP, thereby forcing the protein into a long-lived extended state and preventing it from getting into the contracted state.

We anticipate that our findings are not only key to a better understanding of the Hsp90 machinery, but will contribute to generally recognise the allosteric information transfer through proteins. Last but not least, the presented combination of smFRET, FCS and lifetime measurements with MD simulations holds the promise to investigate time-resolved molecular mechanisms of allostery in many other biomolecular systems.

IV. METHODS

Biochemistry and sample preparation. Yeast Hsp90 was recombinantly produced in *E. coli* and purified as described before.[69] Point mutations were inserted into the yeast Hsp90 gene to obtain single cysteines variants. Fluorescent labels were site-specifically introduced by cysteine-maleimide chemistry. We used ATTO550 as donor and ATTO647N as acceptor fluorophore, respectively (ATTO-TEC, Siegen, Germany). An inserted coiled-coil motif (DmKHC, *D. melanogaster*) at the C-terminus of Hsp90 prevented dimer dissociation and therefore increased the local concentration as we have shown before.[41] To obtain heterodimers which

contain only one donor and one acceptor fluorophore, homodimers with the respective dye were mixed in an 1:1 ratio and incubated for 40 min at 43°C. This enabled a monomor-monomer exchange stochastically leading to 1/2 heterodimers and 1/2 homodimers. To remove aggregates, samples were centrifuged for 1h at 4°C and 16900 g. We applied size exclusion chromatography (SEC) to check that the amount of possibly remaining aggregates is sufficiently low (see Supplement Fig. 10for details). The biofunctionality of the new variant was tested by ATPase assays (see Supplement Fig. 11).

smFRET measurements. Single molecule measurements were carried out on an home-build confocal microscope as depicted in Supplementary Fig. 12. Pulsed green and red laser light (532nm, LDH-P-FA-530 and 640nm, LDH-D-C-640, respectively, PicoQuant) was polarised, overlayed and focused on the sample by an 60x water immersion objective (CFI Plan Apo VC 60XC/1.2 WI, Nikon). Excitation light was separated from the emitted light by a dichroic mirror (F53-534 Dual Line beam splitter z 532/633, AHF). The emitted light was then guided through a further dichroic mirror (F33-647 beam splitter 640 DCXR, AHF) to separate donor and acceptor fluorescence. After spectral separation pinholes with a diameter of 150μm refined the detection volume to 8fL. Finally, the two photon streams were separated by polarizing beam splitters into their parallel and perpendicular parts and recorded by single-photon detectors (two SPCM-AQR-14, PerkinElmer and two PDM-series APDs, Micro Photon Devices). Time-correlated single photon counting with picosecond resolution and data collection was performed by a HydraHarp400 (PicoQuant) and the Symphotime 32 software (PicoQuant). To reach the single-molecule level we adjusted the protein concentration to about 50 pM. Measurements were recorded for 1800s. All experiments were carried out at 22°C in 40 mM HEPES, 150 mM KCl and 10mM $MgCl_2$ at pH=7.5. ADP and ATP were added to the protein solution directly before the measurement, in case of AMPPNP and ATPγS, the samples were pre-incubated for 30 minutes. Nucleotides were added such that their final concentration was 2 mM.

smFRET data analysis. Donor and acceptor photon streams were collected into 1 ms bins. Bursts were selected by a minimum threshold of 100 photons. For every burst the FRET efficiency E and a stoichiometry S was determined as detailed in Ref. 31. FRET populations were determined within the region of $0.3 < S < 0.7$ of corrected E vs S plots. From the FRET efficiency an apparent donor-acceptor distance $R_{\langle E\rangle}$ between the two dyes is determined as[31]

$$R_{\langle E\rangle} = R_0 \left(E^{-1} - 1\right)^{\frac{1}{6}}, \tag{1}$$

where R_0 denotes the Förster radius. We use the efficiency-averaged apparent distance $R_{\langle E\rangle}$, because we assume that during a burst the complete accessible volume of the respective dye is sampled homogeneously, i.e., E is already an average efficiency. $R_{\langle E\rangle}$ can be calculated by the FPS software[70] as is visualized in Supplementary Fig. 13. Note that $R_{\langle E\rangle}$ is also used as a variable for the average from many efficiency averaged bursts, which is only equivalent to $R_{\langle E\rangle}$ in Equation 1 if protein dynamics is negligible.

For every FRET label pair, the Förster radius R_0 was calculated from the donor quantum efficiency Q_{D}, the spectral overlap J, and the relative dipole orientation factor κ^2

$$R_0^6 \propto \kappa^2\, Q_{\mathrm{D}}\, J. \tag{2}$$

Here the dipole orientation factor is assumed to be $\langle\kappa^2\rangle = 2/3$ for isotropic coupling. The position-specific donor quantum yield Q_{D} is given in terms of in dependence of the measured lifetime τ_{D} as well as the parameters Q_{D0} and lifetime τ_{D0} specified by the manufacturer[23] as

$$Q_{\mathrm{D}} = Q_{\mathrm{D0}} \frac{\tau_{\mathrm{D}}}{\tau_{\mathrm{D0}}}. \tag{3}$$

Based on the efficiency distributions (see Fig. 2) and the respective $R_{\langle E\rangle}$ distribution, we determined the expectation value μ of the distance between the two dyes and the apparent distance fluctuation σ via a Photon Distribution Analysis (PDA).[39,40] To that end, we fitted a shot-noise-broadened sum of Gaussian distance distributions to our E histogram, and performed an axis transformation from E-space to $R_{\langle E\rangle}$-space via Equation (1). Specifically, we transform only the bin edges. The Gaussian distance fraction of each histogram bin is obtained by integrating from the left to the right edge and extracting the mean distance. Additionally, the E-specific shot-noise contribution is calculated for each bin, which can be described by a beta-function. We derive its parameters from the number of photons per burst, direct excitation and leakage similar to Ref. 40. The final convolution is gained by simply summing all bin-wise shot-noise beta-functions weighted with the value of the Gaussians for each bin. This essentially assumes a distance delta-function (no protein dynamics) for each bin that undergoes a broadening by shot-noise, which simplifies the convolution greatly. The amplitudes, mean values μ and width σ_{Gauss} of each Gaussian are then optimised by minimising the squared residuals between data and fit. Static and dynamic FRET lines were calculated as detailed in Refs. 62 and 63. To reveal sub-ms kinetics within the Hsp90 dimer, FRET efficiency E vs donor lifetime $\tau_{\mathrm{D(A)}}$ plots were calculated by the PAM software[71] and analysed according to Refs. 70 and 63.

Uncertainties in single-molecule experiments. The widths of the shot-noise-broadened Gaussian fits is caused by shot-noise and structural fluctuations of the protein itself. While σ_{Gauss} is therefore not directly related to an uncertainty of the mean value μ, in our case it is a good indication for the uncertainty of the fit. In addition, in Fig.3 we indicate a minimum uncertainty of 0.36 nm based on findings from structural remodelling.[23]

Analysis of FRET-FCS experiments. FRET-FCS measurements were carried out for FRET pairs 327-452 and 298-452 under ATP, ADP, AMPPNP and apo condition. Protein concentrations were in the range from 0.5 to 1.5 nM and nucleotides were added such that the final concentration was 2mM. Each measurement was recorded for at least 600s and repeated at least once. Cross-correlations Don | x Don ⊥, FRET ∥ x FRET ⊥ and FRET ∥ x Don ⊥ were calculated by the PAM software[71]. Here, 'Don' denotes the photon stream detected in the green channel after green excitation and 'FRET' stands for the photon stream detected in the red detection channel after green excitation. To circumvent artifacts caused by detector afterpulsing we correlated parallel parts ∥ with perpendicular parts ⊥ of the respective photon streams. A software-integrated algorithm was used to remove big aggregates. Cross-correlations were fit by a model assuming simple 3D diffusion and two additional kinetic terms:

$$G(\tau) = \frac{\gamma}{N}\left(1 + Ke^{-\frac{\tau}{\tau_K}} + Le^{-\frac{\tau}{\tau_L}}\right) \cdot \left(1+\frac{\tau}{\tau_D}\right)^{-1}\left(1+\frac{\tau}{\rho^2\tau_D}\right)^{-0.5} + const. \quad (4)$$

Here, γ considers the Gaussian shape of the observation volume, N is the average number of particles within the effective volume, ρ is the ratio of the axial and lateral focus length and τ_D the diffusion time. The two kinetic terms are characterised by their relative weights K and L and their relaxation times τ_K and τ_L. Torres et al. showed, that conformational dynamics and diffusive dynamics can be separated by dividing any two cross-correlations obtained from the same experiment[64]. Similar to Barth et al. we exploited this fact by linking τ_K and τ_L globally[72]. We finally extracted τ_K, K, τ_L and L.

Protein modeling. The yeast wild type Hsp90 dimer model was created by applying MODELLER[73] to one Hsp90 monomer (chain A) from the yeast Hsp90 crystal structure (PDB ID 2CG9)[15] to add missing loops and revert point mutations. The dimer was then reconstituted in vmd[74] by copying the full length monomer and aligning both monomers with the protein backbone of 2CG9. ATP was introduced into the binding site according to the coordinates in 2CG9. We need to point out that this crystal structure does contain ATP coordinates, but was actually crystallized using AMPPNP. For modeling structures with bound ADP and phosphate, we manually introduced a geometry change of the ATP γ-phosphate as it should appear in a S_N2 nucleophilic attack by a water molecule. The resulting ADP + Pi complex thus represents a structure immediately after the hydrolysis reaction and before any relaxation of the protein.

MD simulations and data analysis. All simulations of the Hsp90 dimer water were carried out using Gromacs 2016 (Ref. 75) using the Amber99SB*ILDN-parmbsc0-$_{\chi OL3}$ + AMBER99ATP/ADP force field.[76] ATP/ADP and phosphate parameters were derived from Refs. 77 and 78. Missing $H_2PO_4^-$ and AMPPNP parameters were generated based on a protocol we have used before.[79] A detailed explanation of the force field used, the parameter generation procedure, and the simulation parameters used is given in the Supplementary Information. Simulation boxes were first minimised using the conjugate gradient method with position restraints on protein, nucleotide and phosphate heavy atoms. By starting with different initial velocity distributions, five statistically independent simulation replicas were calculated for each nucleotide load investigated. After a first 100 ps equilibration simulation with position restraints, each unbiased equilibrium production simulation was run for a total trajectory length of 1 µs. Simulations with modelled hydrolysis were subjected to a second equilibration run of 100 ps trajectory length with a step size of 0.2 fs and removed restraints to allow the binding site to adjust to the presence of the free phosphate molecule.

Interprotein distances were assessed using a correlation-based contact principal component analysis (conPCA)[53,54] on the last 0.5 µs of each simulation. We took into account all minimal interresidue distances $\mathbf{d} = \{d_{ij}\}$ within and between the N-domain and M-loops that lie within a 0.45 nm cutoff in the final structures after 1 µs of all 25 simulations. conPCA builds a correlation matrix

$$\sigma_{ij} = \langle d_i - \langle d_i \rangle \rangle \langle d_j - \langle d_j \rangle \rangle / \sigma_i \sigma_j, \quad (5)$$

with distance variances σ_i and σ_j which after diagonalisation yields n eigenvectors $\mathbf{e^{(n)}}$ that are aligned with the maximal correlation within the data set, and n eigenvalues $v^{(n)}$ that determine the contribution of eigenvector n to the overall correlation. The principal components PC_n are then obtained via the projection

$$PC_n = \mathbf{e^{(n)}} \cdot \mathbf{d}. \quad (6)$$

Visualization of molecular data was performed with vmd.[74]

For nonequilibrium targeted molecular dynamics simulations,[51,52] we employed the PULL code from Gromacs. Prior to these simulations, we removed bulk solvent and ions from the final structure of one of the ADP+P_i simulations after 1 µs simulation time, mimicking the influence of water by setting the relative permittivity $\epsilon_r = 78$ in the simulation, while lowering the overall friction of the system. For a simulation length length of 1 ns, we pulled the C_β atoms of the distance pairs 298-327, 298-452 and 327-452 with a constant constraint velocity of 1 m/s, 2 m/s and 1 m/s, respectively, which roughly corresponds to the changes in $R_{\langle E \rangle}$ observed between closed states A and B (see Fig. 4a). We then use the apparent distances of $R_{\langle E \rangle}$ as read-out parameter, as they are derived from fluorophore accessible

volume, and not the C_β distance. Additionally, we did not manipulate 142-597, but use it as a control parameter.

Comparing smFRET data to MD simulation data. Usually, FRET experiments and MD simulations are compared by converting dye distances into C_β-atom distances, using geometric arguments concerning linker lengths and flexibility. Since the latter usually involves ill-defined assumptions, we instead compared measured and calculated $R_{\langle E \rangle}$. That is, we directly calculate the expected $R_{\langle E \rangle}$ for each simulations snapshot using the FPS software,[70] which analyses the volume a dye can access within the linker length around a given C_β-atom.[31,80] This yields the $R_{\langle E \rangle}$ distributions shown in Fig. 4a, which can be directly compared to the mean experimental distance μ. The approach assumes isotropic averaging of dipoles during FRET, which can be verified via the low combined anisotropy of the FRET dyes (see Supplementary Tab. 1 and Ref. 31). Even in case of partial anisotropic averaging, this approach is preferential over simple C_β estimation, as the volumes accessible to the fluorophores significantly depend on the structures appearing during the MD simulation.

DATA AVAILABILITY

Final MD structures of the 1 μs simulation runs are available with the online version of this manuscript. Additional data such as MD trajectories can be obtained from the authors upon request. The PCA software *fastpca* is available under `https://www.moldyn.uni-freiburg.de/software/software.html` or directly at `https://moldyn.github.io/FastPCA/`.

REFERENCES

[1] Motlagh, H. N., Wrabl, J. O., Li, J. & Hilser, V. J. The ensemble nature of allostery. *Nature (London)* **508**, 331 – 339 (2014).

[2] Nussinov, R. Special issue on protein ensembles and allostery. *Chem. Rev.* **116**, 6263–6266 (2016).

[3] Wodak, S. J. *et al.* Allostery in Its Many Disguises: From Theory to Applications. *Structure* **27**, 566–578 (2019).

[4] Kern, D. & Zuiderweg, E. The role of dynamics in allosteric regulation. *Curr. Opin. Struct. Biol.* **13**, 748–757 (2003).

[5] Brüschweiler, S. *et al.* Direct observation of the dynamic process underlying allosteric signal transmission. *J. Am. Chem. Soc.* **131**, 3063–3068 (2009).

[6] Buchli, B. *et al.* Kinetic response of a photoperturbed allosteric protein. *Proc. Natl. Acad. Sci. USA* **110**, 11725–11730 (2013).

[7] Pontiggia, F. *et al.* Free energy landscape of activation in a signalling protein at atomic resolution. *Nat. Comm.* **6**, 7284 (2015).

[8] Buchenberg, S., Sittel, F. & Stock, G. Time-resolved observation of protein allosteric communication. *Proc. Natl. Acad. Sci. U.S.A.* **114**, 201707694–E6811 (2017).

[9] Nussinov, R. & Tsai, C.-J. Allostery in Disease and in Drug Discovery. *Cell* **153**, 293–305 (2013).

[10] Abdel-Magid, A. F. Allosteric Modulators: An Emerging Concept in Drug Discovery. *ACS Med. Chem. Lett.* **6**, 104–107 (2015).

[11] Pearl, L. H. & Prodromou, C. Structure and Mechanism of the Hsp90 Molecular Chaperone Machinery. *Annu. Rev. Biochem.* **75**, 271–294 (2006).

[12] Schopf, F. H., Biebl, M. M. & Buchner, J. The HSP90 chaperone machinery. *Nat. Rev. Mol. Cell Biol.* **18**, 345–360 (2017).

[13] Whitesell, L. & Lindquist, S. L. HSP90 and the chaperoning of cancer. *Nat. Rev. Cancer* **5**, 761–772 (2005).

[14] Blagg, B. S. J. & Kerr, T. D. Hsp90 inhibitors: Small molecules that transform the Hsp90 protein folding machinery into a catalyst for protein degradation. *Med. Res. Rev.* **26**, 310–338 (2006).

[15] Ali, M. M. U. *et al.* Crystal structure of an Hsp90-nucleotide-p23/Sba1 closed chaperone complex. *Nature* **440**, 1013–1017 (2006).

[16] Huck, J. D., Que, N. L., Hong, F., Li, Z. & Gewirth, D. T. Structural and Functional Analysis of GRP94 in the Closed State Reveals an Essential Role for the Pre-N Domain and a Potential Client-Binding Site. *Cell Rep.* **20**, 2800–2809 (2017).

[17] Lavery, L. A. *et al.* Structural Asymmetry in the Closed State of Mitochondrial Hsp90 (TRAP1) Supports a Two-Step ATP Hydrolysis Mechanism. *Mol. Cell* **53**, 330–343 (2014).

[18] Verba, K. A. *et al.* Atomic structure of Hsp90-Cdc37-Cdk4 reveals that Hsp90 traps and stabilizes an unfolded kinase. *Science* **352**, 1542–1547 (2016).

[19] Dollins, D. E., Warren, J. J., Immormino, R. M. & Gewirth, D. T. Structures of GRP94-nucleotide complexes reveal mechanistic differences between the hsp90 chaperones. *Mol. Cell* **28**, 41–56 (2007).

[20] Seifert, C. & Gräter, F. Force Distribution Reveals Signal Transduction in E. coli Hsp90. *Biophys. J.* **103**, 2195–2202 (2012).

[21] Morra, G., Potestio, R., Micheletti, C. & Colombo, G. Corresponding Functional Dynamics across the Hsp90 Chaperone Family: Insights from a Multiscale Analysis of MD Simulations. *PLoS Comput. Biol.* **8**, e1002433 (2012).

[22] Simunovic, M. & Voth, G. A. Molecular and Thermodynamic Insights into the Conformational Transitions of Hsp90. *Biophys. J.* **103**, 284–292 (2012).

[23] Hellenkamp, B., Wortmann, P., Kandzia, F., Zacharias, M. & Hugel, T. Multidomain structure and correlated dynamics determined by self-consistent FRET networks. *Nat. Methods* **14**, 174–180 (2017).

[24] Pearl, L. H. The HSP90 molecular chaperone-an enigmatic ATPase. *Biopolymers* **105**, 594–607 (2016).

[25] Ha, T. *et al.* Probing the interaction between two single molecules: fluorescence resonance energy transfer between a single donor and a single acceptor. *Proc. Natl. Acad. Sci. USA* **93**, 6264–6268 (1996).

[26] Muschielok, A. *et al.* A nano-positioning system for macromolecular structural analysis. *Nat. Methods* **5**, 965–971 (2008).

[27] Brunger, A. T., Strop, P., Vrljic, M., Chu, S. & Weninger, K. R. Three-dimensional molecular modeling with single molecule FRET. *J. Struct. Biol.* **173**, 497–505 (2011).

[28] Kityk, R., Vogel, M., Schlecht, R., Bukau, B. & Mayer, M. P. Pathways of allosteric regulation in Hsp70 chaperones. *Nat. Commun.* **6**, 1 (2015).

[29] Zosel, F., Mercadante, D., Nettels, D. & Schuler, B. A proline switch explains kinetic heterogeneity in a coupled folding and binding reaction. *Nat. Commun.* **9**, 3332 (2018).

[30] Lerner, E. *et al.* Toward dynamic structural biology: Two decades of single-molecule Förster resonance energy transfer. *Science* **359**, eaan1133 (2018).

[31] Hellenkamp, B. *et al.* Precision and accuracy of single-molecule fret measurementsa multi-laboratory benchmark study. *Nat. Methods* **15**, 669 (2018).

[32] Sisamakis, E., Valeri, A., Kalinin, S., Rothwell, P. J. & Seidel, C. A. M. Accurate Single-Molecule FRET Studies Using Multiparameter Fluorescence Detection. In *Single Molecule Tools, Part B:Super-Resolution, Particle Tracking, Multiparameter, and Force Based Methods*, 455–514 (Elsevier, 2010).

[33] Schröder, G. F., Alexiev, U. & Grubmüller, H. Simulation of Fluorescence Anisotropy Experiments: Probing Protein Dynamics.

Biophys. J. **89**, 3757–3770 (2005).
[34]Best, R. B., Hofmann, H., Nettels, D. & Schuler, B. Quantitative Interpretation of FRET Experiments via Molecular Simulation: Force Field and Validation. *Biophys. J.* **108**, 2721–2731 (2015).
[35]Reinartz, I. *et al.* Simulation of FRET dyes allows quantitative comparison against experimental data. *J. Chem. Phys.* **148**, 123321 (2018).
[36]Cunningham, C. N., Southworth, D. R., Krukenberg, K. A. & Agard, D. A. The conserved arginine 380 of Hsp90 is not a catalytic residue, but stabilizes the closed conformation required for ATP hydrolysis. *Protein Sci.* **21**, 1162–1171 (2012).
[37]Schulze, A. *et al.* Cooperation of local motions in the Hsp90 molecular chaperone ATPase mechanism. *Nat. Chem. Biol.* **12**, 628–635 (2016).
[38]Lee, B. L., Rashid, S., Wajda, B., Biochemistry, A. W. & 2019. The Hsp90 Chaperone: 1H and 19F Dynamic Nuclear Magnetic Resonance Spectroscopy Reveals a Perfect Enzyme. *Biochemistry* **58**, 1869–1877 (2019).
[39]Antonik, M., Felekyan, S., Gaiduk, A. & Seidel, C. A. M. Separating structural heterogeneities from stochastic variations in fluorescence resonance energy transfer distributions via photon distribution analysis. *J. Phys. Chem. B* **110**, 6970–6978 (2006).
[40]Nir, E. *et al.* Shot-Noise Limited Single-Molecule FRET Histograms: Comparison between Theory and Experiments . *J. Phys. Chem. B* **110**, 22103–22124 (2006).
[41]Mickler, M., Hessling, M., Ratzke, C., Buchner, J. & Hugel, T. The large conformational changes of hsp90 are only weakly coupled to atp hydrolysis. *Nat. Struct. Mol. Biol.* **16**, 281 (2009).
[42]Schmid, S., Goetz, M. & Hugel, T. Single-Molecule Analysis beyond Dwell Times: Demonstration and Assessment in and out of Equilibrium. *Biophys. J.* **111**, 1375–1384 (2016).
[43]Giannoulis, A. *et al.* Two closed atp- and adp-dependent conformations in yeast hsp90 chaperone detected by mn(ii) epr spectroscopic techniques. *Proc. Natl. Acad. Sci. USA* **117**, 395–404 (2020).
[44]Street, T. O. *et al.* Cross monomer substrate contacts reposition the Hsp90 N-terminal domain and prime the chaperone activity. *J. Mol. Biol.* **415**, 3–15 (2012).
[45]Huang, B., Friedman, L. J., Sun, M., Gelles, J. & Street, T. O. Conformational Cycling within the Closed State of Grp94, an Hsp90-Family Chaperone. *J. Mol. Biol.* **431**, 3312–3323 (2019).
[46]Ratzke, C., Berkemeier, F. & Hugel, T. Heat shock protein 90's mechanochemical cycle is dominated by thermal fluctuations. *Proc. Natl. Acad. Sci. U.S.A.* **109**, 161–166 (2012).
[47]Panaretou, B. *et al.* ATP binding and hydrolysis are essential to the function of the Hsp90 molecular chaperone in vivo. *EMBO J.* **17**, 4829–4836 (1998).
[48]Roe, S. M. *et al.* The Mechanism of Hsp90 Regulation bythe Protein Kinase-Specific Cochaperone p50. *Cell* **116**, 87–98 (2014).
[49]Prodromou, C. Mechanisms of Hsp90 regulation. *Biochem. J.* **473**, 2439–2452 (2016).
[50]Meyer, P. *et al.* Structural and functional analysis of the middle segment of Hsp90: Implications for ATP hydrolysis and client protein and cochaperone interactions. *Mol. Cell* **11**, 647–658 (2003).
[51]Schlitter, J., Engels, M. & Krüger, P. Targeted molecular dynamics - a new approach for searching pathways of conformational transitions. *J. Mol. Graph.* **12**, 84–89 (1994).
[52]Wolf, S. *et al.* Estimation of Protein-Ligand Unbinding Kinetics Using Non-Equilibrium Targeted Molecular Dynamics Simulations. *J. Chem. Inf. Model.* **59**, 5135–5147 (2019).
[53]Ernst, M., Sittel, F. & Stock, G. Contact- and distance-based principal component analysis of protein dynamics. *J. Chem. Phys.* **143**, 244114 (2015).
[54]Ernst, M., Wolf, S. & Stock, G. Identification and Validation of Reaction Coordinates Describing Protein Functional Motion: Hierarchical Dynamics of T4 Lysozyme. *J. Chem. Theory Comput.* **13**, 5076–5088 (2017).
[55]Retzlaff, M. *et al.* Asymmetric Activation of the Hsp90 Dimer by Its Cochaperone Aha1. *Mol. Cell* **37**, 344–354 (2010).
[56]Flynn, J. M., Mishra, P. & Bolon, D. N. A. Mechanistic Asymmetry in Hsp90 Dimers. *J. Mol. Biol.* **427**, 2904–2911 (2015).
[57]Vetter, I. R. & Wittinghofer, A. The guanine nucleotide-binding switch in three dimensions. *Science* **294**, 1299–1304 (2001).
[58]Penkler, D. L., Atilgan, C. & Tastan Bishop, Ö. Allosteric Modulation of Human Hsp90α Conformational Dynamics. *J. Chem. Inf. Model.* **58**, 383–404 (2018).
[59]Zierer, B. K. *et al.* Importance of cycle timing for the function of the molecular chaperone Hsp90. *Nat. Struct. Mol. Biol.* **23**, 1020–1028 (2016).
[60]Henzler-Wildman, K. A. *et al.* A hierarchy of timescales in protein dynamics is linked to enzyme catalysis. *Nature (London)* **450**, 913–916 (2007).
[61]Buchenberg, S., Schaudinnus, N. & Stock, G. Hierarchical biomolecular dynamics: Picosecond hydrogen bonding regulates microsecond conformational transitions. *J. Chem. Theory Comput.* **11**, 1330–1336 (2015).
[62]Kalinin, S., Valeri, A., Antonik, M., Felekyan, S. & Seidel, C. A. M. Detection of Structural Dynamics by FRET: A Photon Distribution and Fluorescence Lifetime Analysis of Systems with Multiple States. *J. Phys. Chem. B* **114**, 7983–7995 (2010).
[63]Gopich, I. V. & Szabo, A. Theory of the energy transfer efficiency and fluorescence lifetime distribution in single-molecule FRET. *Proc. Natl. Acad. Sci. USA* **109**, 7747–7752 (2012).
[64]Torres, T. & Levitus, M. Measuring conformational dynamics: A new fcs-fret approach. *J. Phys. Chem. B* **111**, 7392–7400 (2007).
[65]Felekyan, S., Sanabria, H., Kalinin, S., Künemuth, R. & Seidel, C. A. Analyzing förster resonance energy transfer with fluctuation algorithms. In *Methods Enzymol.*, vol. 519, 39–85 (Elsevier, 2013).
[66]Barth, A. *et al.* Dynamic interactions of type I cohesin modules fine-tune the structure of the cellulosome of Clostridium thermocellum. *Proc. Natl. Acad. Sci. USA* **115**, E11274–E11283 (2019).
[67]Rutz, D. A. *et al.* A switch point in the molecular chaperone Hsp90 responding to client interaction. *Nat. Commun.* **9**, 1–14 (2018).
[68]Rehn, A. *et al.* A methylated lysine is a switch point for conformational communication in the chaperone Hsp90. *Nat. Commun.* **11**, 1–14 (2020).
[69]Götz, M., Wortmann, P., Schmid, S. & Hugel, T. A multicolor single-molecule fret approach to study protein dynamics and interactions simultaneously. In *Methods Enzymol.*, vol. 581, 487–516 (Elsevier, 2016).
[70]Kalinin, S. *et al.* A toolkit and benchmark study for fret-restrained high-precision structural modeling. *Nat. Methods* **9**, 1218 (2012).
[71]Schrimpf, W., Barth, A., Hendrix, J. & Lamb, D. C. Pam: A framework for integrated analysis of imaging, single-molecule, and ensemble fluorescence data. *Biophys. J.* **114**, 1518–1528 (2018).
[72]Barth, A. *et al.* Dynamic interactions of type i cohesin modules fine-tune the structure of the cellulosome of clostridium thermocellum. *Proc. Natl. Acad. Sci. USA* **115**, E11274–E11283 (2018).
[73]Webb, B. & Sali, A. Comparative Protein Structure Modeling Using MODELLER. *Curr. Protoc. Bioinformatics* **47**, 5.6.1–5.6.32 (2014).
[74]Humphrey, W., Dalke, A. & Schulten, K. VMD – Visual Molecular Dynamics. *J. Mol. Graph.* **14**, 33–38 (1996).
[75]Abraham, M. J. *et al.* GROMACS: High performance molecular simulations through multi-level parallelism from laptops to supercomputers. *SoftwareX* **1**, 19–25 (2015).
[76]Pérez-Villa, A., Darvas, M. & Bussi, G. ATP dependent NS3 helicase interaction with RNA: insights from molecular simulations. *Nucleic Acids Res.* **43**, 8725–8734 (2015).
[77]Meagher, K. L., Redman, L. T. & Carlson, H. A. Development of polyphosphate parameters for use with the AMBER force field. *J. Comput. Chem.* **24**, 1016–1025 (2003).
[78]Pérez, A. *et al.* Refinement of the AMBER force field for nucleic acids: improving the description of alpha/gamma conformers. *Biophys. J.* **92**, 3817–3829 (2007).

[79] Zanobini, C. *et al.* Azidohomoalanine: A Minimally Invasive, Versatile, and Sensitive Infrared Label in Proteins To Study Ligand Binding. *J. Phys. Chem. B* **122**, 10118–10125 (2018).
[80] Sindbert, S. *et al.* Accurate Distance Determination of Nucleic Acids via Förster Resonance Energy Transfer: Implications of Dye Linker Length and Rigidity. *J. Am. Chem. Soc.* **133**, 2463–2480 (2011).

ACKNOWLEDGMENTS

This work has been supported by the European Research Council through ERC grant agreement No. 681891, and by the German Research Foundation (DFG) under Germany's Excellence Strategy (CIBSS EXC-2189 Project ID 390939984) and through grant No. Sto 247/10-2. The authors acknowledge support by the bwUniCluster computing initiative, the High Performance and Cloud Computing Group at the Zentrum für Datenverarbeitung of the University of Tübingen, the state of Baden-Württemberg through bwHPC and the German Research Foundation (DFG) through grant No. INST 37/935-1 FUGG, and by the Freiburg Institute for Advanced Studies (FRIAS). TH thanks Timothy Street for helpful discussions.

AUTHOR CONTRIBUTIONS

S.W., B.H., G.S. and T.H. designed and guided research; S.W. carried out and analysed simulations; B.S. performed and analysed smFRET and FCS experiments with help from J.T. and B.H.; S.W., B.S., B.H., G.S. and T.H. wrote the manuscript.
† These authors contributed equally.

CORRESPONDING AUTHORS

*steffen.wolf@physik.uni-freiburg.de
*b.hellenkamp@columbia.edu
*thorsten.hugel@physchem.uni-freiburg.de

ADDITIONAL INFORMATION

Supplementary Information

Supplementary Methods, two Supplementary Tables, thirteen Supplementary Figures, three Supplementary Notes, one Supplementary Structure set and one Supplementary Movie are available with the online version of this manuscript.

Competing Interests

The authors declare no competing interests.

Author ORCID IDs

Steffen Wolf: 0000-0003-1752-6175
Benedikt Sohmen: 0000-0002-7103-3788
Björn Hellenkamp: 0000-0001-7623-1452
Johann Thurn: 0000-0001-6370-7052
Gerhard Stock: 0000-0002-3302-3044
Thorsten Hugel: 0000-0003-3292-4569